Research Article

Samira Elaissi* and Norah A. M. Alsaif

Numerical modeling of enhanced reactive oxygen plasma in pulsed laser deposition of metal oxide thin films

https://doi.org/10.1515/phys-2025-0197 received April 05, 2025; accepted June 03, 2025

Abstract: Metal oxide films have received a lot of scientific research interest over the past few years because of their excellent optical and electrical properties needed for optoelectronic devices as well as their low cost and nontoxicity. Plasma enhanced-pulsed laser deposition (PE-PLD) is utilized for the growth of thin films on flexible, thermally sensitive polymer surfaces. A background oxygen plasma gas is required for PLD to enhance the control process and to prevent oxygen deficiency during metal oxide film formation. Simulation results using COMSOL Multiphysics show that a radiofrequency-driven inductively coupled plasma (ICP) model generates reactive oxygen species, like O and O₂*, with densities of 10¹⁹–10²⁰ m⁻³, which significantly affect film deposition. As the applied power and pressures are increased, the electron temperature decreases and the oxygen ion density diminishes, which enhances the deposition rate and minimizes defects in oxide films. Furthermore, as power increases, oxygen atoms gain energy leading to higher atom excitation, while increasing pressure declines the total ion flux. Also, the crystal construction, stoichiometry, and characteristics of the metal oxide films on polymer foils are affected by the O/O₂ ratio. Based on the numerical model developed in this article, stoichiometric metal oxide thin films are achieved, and materials are transferred to polymer substrates at high rates.

Keywords: oxygen ICP plasma, thin film growth, stoichiometry, plasma parameters, deposition rate

1 Introduction

Metal oxide materials, such as copper oxides (CuO and Cu₂O) and zinc oxide (ZnO), have been the subject of extensive research in recent decades for their unique optical, electrical, chemical, and electronic properties. Copper oxide thin films (CuO and Cu₂O) are p-type semiconductors that find applications in thin film transistors, solar cells, supercapacitors, and gas sensors [1]. In addition, ZnO is an n-type semiconductor with a wide bandgap of 3.3 eV, a high melting point at 2,000°C, and elevated exciton binding energy. Due to their non-toxicity, low cost, and ecofriendliness [2], ZnO films are mainly investigated for many applications, such as solar cells, polymer coating, antibacterial agents, microelectronics, and optical waveguides [3]. Despite the variety of metal oxide applications, the film quality, substrate temperature, and control of stoichiometry remain challenging issues. Hence, controlled and more complex processes are required to produce highquality metal oxide thin films [4,5].

Thermo-evaporation is easy to use and reasonably priced but may not be feasible without a high enough temperature and good supply of electricity. Moreover, thin films cannot adhere effectively to surfaces during thermal deposition, and their thickness and composition are difficult to control [6]. In contrast, excellent film uniformity and composition control are provided by sputtering, which blasts atoms or molecules out of a target substance using high-energy ions and then deposits them onto a substrate. However, it takes time and has complicated equipment [7]. The chemical vapor deposition (CVD) which combines gases on a surface to form a solid layer can provide exact control over composition and thickness. Nonetheless, CVD is expensive, requires specialized equipment, and uses high temperatures. Additionally, many chemical precursors employed in CVD are extremely hazardous [8].

In comparison, pulsed laser deposition (PLD) offers distinct advantages over the other deposition methods [9] with outstanding adhesion, superior quality, and precise

^{*} Corresponding author: Samira Elaissi, Department of Physics, College of Science, Princess Nourah Bint Abdulrahman University, P.O. Box 84428, Riyadh, 11671, Saudi Arabia, e-mail: saelaissi@pnu.edu.sa Norah A. M. Alsaif: Department of Physics, College of Science, Princess Nourah Bint Abdulrahman University, P.O. Box 84428, Riyadh, 11671, Saudi Arabia

composition control. It is a very adaptable process and can deposit a wide variety of materials, including complex chemicals and multilayer structures with limited stoichiometry control, high deposition rates, and easy material interchangeability. Despite their advantages, these methods utilize higher substrate temperatures for film deposition and sample post-treatment on sapphire or glass surfaces.

Solar cells and plastic electronic devices require the use of pure ZnO or aluminum-doped ZnO films generated on flexible, thermally sensitive polymer substrates like polyethylene terephthalate [10]. Hence, different additives have been increasingly used to enhance film growth, such as the use of plasmas to produce reactive species during film deposition [11]. Alternatively, reactive oxygen plasma at low temperatures is used to enhance PLD, a process recognized as plasma-enhanced pulsed laser deposition (PE-PLD) [12]. This technology intends to improve stoichiometric control of thin layers from the target material to the substrate by combining a typical PLD setup with a lowtemperature, electrically generated oxygen plasma. During deposition, a mixture of ions, atoms, and neutral oxygen molecules is produced in the background plasma independent of interaction with the ablation plume, allowing surface reorganization and preparation. This is beneficial to prevent the production of oxygen-deficient metal oxide coatings which can be deposited on flexible plastic substrates without substrate heating or film annealing [13]. Also, metal targets are simpler to manage and cheaper to produce than oxides or compound targets, and the radiofrequency (RF) plasma offers more control over the growth of the film. Further, control of the structure and expansion of the plume during the process of ablation are feasible, and the system can also be expanded to include other gases for achieving more diverse films (like N₂ for nitrides) [14].

However, PE-PLD still has some disadvantages, such as greater expense and complexity, and a restricted deposition area. So, this field remains under research because of its intricacy and unclear process definitions. According to Huang et al. [15], radiofrequency parallel plate discharge is used as the PLD background. Also, ZnO films are observed with a (0 02) c-axis direction and higher deposition rates than the traditional PLD. Scarisorneau et al. [16] have used an oxygen plasma source to deposit thin oxide films. They have demonstrated that by altering oxygen plasma beam relative orientations, different crystal orientations could be obtained. With the use of a directional RF plasma beam over a PLD setup, Nistor et al. [17] have demonstrated that high quality c-axis and a-axis ZnO films can be grown. This research has focused on the film generation by oxygen plasma, rather than analyzing or modeling the plasma properties.

In this work, the method for PE-PLD of metal oxide films using a heat-sensitive substrate material is presented. A numerical simulation of PE-PLD with RF inductively coupled oxygen plasma is performed through COMSOL Multiphysics [18]. The model using the Gaseous Electronics Conference radiofrequency (GEC-RF) reference cell is employed to examine the quantity and type of deposited oxygen reactive species and to control film crystallization and stoichiometry of metal oxide thin films. Reactive oxygen species are investigated to provide insight into the type and concentration of reactive oxygen species that contribute to thin film formation. Additionally, different operating conditions, like power and pressure deposition and temperature, are explored for analyzing the influence of plasma parameters on oxide thin film deposition on flexible and thermally sensitive polymer substrates. The current article focuses on the optimal operation process for the deposition of metal oxide thin coatings to achieve higher quality of conductive thin coatings adhering to the polymeric substrate and to enhance the structure, morphology, and deposition rate of generated films.

2 PE-PLD process

An experimental setup for PE-PLD for the generation of ZnO films is presented in Figure 1. In this setup, a focused pulsed laser beam is coupled to a stainless-steel vacuum chamber, and the oxygen gas flow into the chamber is controlled with a mechanical pump. In order to ablate the ZnO targets (purity, 99.99%; frequency, 10 Hz), the pulsed laser is operated under the following conditions: pulse energy, 35 mJ; wavelength, 532 nm; pulse duration, 5 ns.

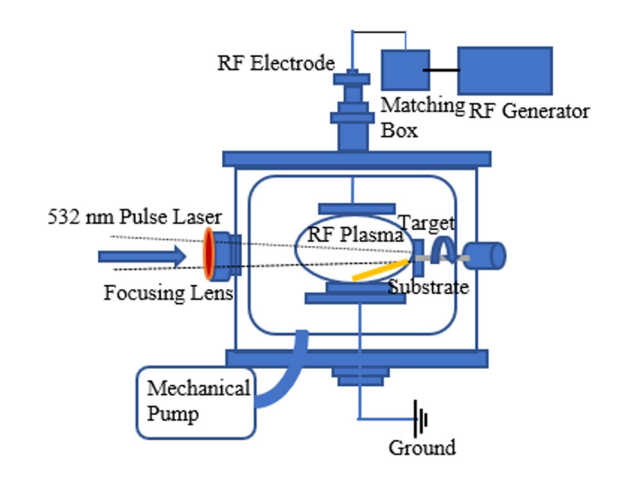


Figure 1: PE-PLD system for thin film deposition.

This wavelength is commonly employed in PLD using the Nd:YAG laser system. A quartz window is used to direct the laser beam at an incident angle of 90° to the target. RF plasma discharge is produced by connecting a 300 W power supply at 13.56 MHz to the top electrode. The target and substrate are separated by 6 cm [19]. Indeed, incorporating oxygen gas into the background atmosphere of PLD enhances the film oxygen content and crystallization structure. Plasma plumes generated by lasers travel through the oxygen background gas and interact with it before being deposited on the substrate. With background gas molecules, complex interactions occur and oxygen molecules are dissociated into highly reactive oxygen atoms interacting with the target or depositing on the substrate [20].

3 Numerical model

A simulation of inductively coupled plasma (ICP) model at low pressure is performed using a 2D fluid model derived from the continuity equation, the mean electron energy equation balance, and Maxwell equations. The plasma module and laminar flow are coupled through Navier–Stokes equations for neutral background gas [21].

3.1 Modeling equations

In terms of electron densities, the continuity equation is defined as follows:

$$\frac{\partial}{\partial t}(n_{\rm e}) + \nabla \cdot \mathbf{\Gamma}_{\rm e} = R_{\rm e},\tag{1}$$

where t is the time, while n_e , Γ_e , and R_e represent, respectively, the electron density, the flux of electrons, and the term source dependent on different chemical reactions included in the deposition process [22].

Drift diffusion equations are used to compute the electron density and average energy of electrons, expressed as follows:

$$\mathbf{\Gamma}_{e} = -n_{e}\mu_{e}\mathbf{E} - D_{e}\nabla n_{e}. \tag{2}$$

Here, $D_{\rm e}$ and $\mu_{\rm e}$ represent the electron diffusion and the electron mobility coefficients, respectively, and ${\bf E}$ is the electric field.

The energy equation for electrons is given by

$$\frac{\partial}{\partial t}(n_{\rm e}\varepsilon) + \nabla \cdot \Gamma_{\varepsilon} + \mathbf{E} \cdot \Gamma_{\rm e} = R_{\varepsilon},\tag{3}$$

$$\mathbf{\Gamma}_{\varepsilon} = -n_{\varepsilon}\mu_{\varepsilon}\mathbf{E} - \mathbf{D}_{\varepsilon}\nabla n_{\varepsilon}. \tag{4}$$

Here, ε and Γ_{ε} represent the mean energy of electrons and the flux of electron energy, respectively, and R_{ε} denotes the source term of electron energy because of inelastic collisions. The energy diffusivity, energy mobility, and electron diffusivity are given by

$$\mu_{\varepsilon} = \left(\frac{5}{3}\right)\mu_{\rm e}, \quad \mathbf{D}_{\varepsilon} = \mu_{\varepsilon}T_{\rm e}, \quad D_{e} = \mu_{\rm e}T_{\rm e},$$
 (5)

where $T_{\rm e}$ represents the temperature of electrons.

The mass fractions of non-electron species are calculated using the following equation:

$$\rho \frac{\partial}{\partial t}(w_k) + \rho(\mathbf{u} \cdot \nabla)w_k = \nabla \cdot \mathbf{J}_k + R_k, \tag{6}$$

$$\mathbf{J}_{\mathbf{k}} = \rho w_k \mathbf{V}_k,\tag{7}$$

$$\mathbf{V}_{k} = D_{k} \left(\frac{\nabla w_{k}}{w_{k}} + \frac{\nabla M_{n}}{M_{n}} \right) - Z_{k} \mu_{k} \mathbf{E}, \tag{8}$$

where ρ , M_n , and \mathbf{u} denote the gas density, the average molar mass, and the average velocity of the gas, respectively. \mathbf{J}_k , w_k , and \mathbf{V}_k are the diffusion flux vector, the mass fraction, and the speed vector, respectively, for non-electron species k. Z_k denotes the charge number, D_k is the diffusion coefficient, μ_k represents the mobility coefficient, and R_k is the source term.

Equations for electromagnetic fields are formulated as follows [23]:

$$\nabla \times \mathbf{E} = i\omega \mathbf{B},\tag{9}$$

$$\frac{1}{\mu_0} \nabla \times \mathbf{B} = \mathbf{J}_{\text{ext}} - i\omega \varepsilon_0 \mathbf{K} \cdot \mathbf{E}, \tag{10}$$

$$\varepsilon_0 \nabla \cdot (\mathbf{K} \cdot \mathbf{E}) = \rho_{\text{ext}}, \tag{11}$$

$$\nabla \cdot \mathbf{B} = 0. \tag{12}$$

In these equations, i, ε_0 , μ_0 , and $\rho_{\rm ext}$ represent, respectively, the imaginary number, the permittivity of free space, the vacuum permeability, and the space charge density expressed on the basis of a chemistry model and given by:

$$\rho_{\text{ext}} = q \left(\sum_{k=1}^{N} Z_k n_k - n_{\text{e}} \right). \tag{13}$$

B is the magnetic field vectors and $\omega = 2\pi f$ denotes the angular frequency, where f represents the electromagnetic field frequency. **K** is the dielectric tensor written as

$$\mathbf{K} = 1 + \frac{i}{\omega \varepsilon_0} \sigma_{\mathbf{p}},\tag{14}$$

where σ_p is the plasma conductivity given by

$$\sigma_{\rm p} = \frac{\varepsilon_0 \omega_{\rm pe}^2}{\vartheta - i\omega},\tag{15}$$

and ω_{pe} is the electron plasma frequency expressed as

$$\omega_{\rm pe} = \sqrt{\frac{n_{\rm e}e^2}{m_{\rm e}\varepsilon_0}} \,. \tag{16}$$

Here, n_e , m_e , ϑ , and e represent, respectively, the period averaged electron density, the electron mass, the total collision frequency, and the electron charge.

Combining Eqs. (9) and (10), the coil current density $\mathbf{J}_{\mathrm{ext}}(s)$ can be calculated as

$$-\nabla \times \nabla \times \mathbf{E} + \frac{\omega^2}{C^2} \mathbf{K} \cdot \mathbf{E} = -i\omega \mu_0 \mathbf{J}_{\mathbf{ext}}(s), \tag{17}$$

where s represents the position along the induction coil, and the capacitive current flowing through the coil I_c can be derived from the volume integral of the charge on the coil

$$\frac{\partial}{\partial s} \left[\int_{A} J_{\text{ext}}(s) \cdot dA \right] \Delta s = I_{\text{c}}(s). \tag{18}$$

For neutral background gas, Navier–Stokes equations are as follows:

Mass conservation:

$$\nabla(\rho \mathbf{u}) = 0. \tag{19}$$

Momentum conservation:

$$\nabla(\rho \mathbf{u}\mathbf{u}) = -\nabla p + \nabla \left[\mu(\nabla \mathbf{u} + \nabla \mathbf{u}^{\mathrm{T}}) - \frac{2}{3}\mu\nabla \cdot (\mathbf{u}\mathbf{I})\right] + F, \quad (20)$$

$$F = \rho g + \mathbf{J} \times \mathbf{B},\tag{21}$$

where \mathbf{u} , T, ρ , μ , p, \mathbf{I} , \mathbf{B} , and \mathbf{J} represent, respectively, the velocity, the temperature, the gas density, the viscosity, the pressure, the density tensor, the magnetic field, and the induced current density in the plasma.

Species on the surface are determined from their deposition height [24]:

$$\frac{\mathrm{d}h}{\mathrm{d}t} = \frac{RM}{\rho_{\rm b}},\tag{22}$$

where h, R, M, and ρ_b , represent, respectively, the total growth height, the surface rate expression, the molecular weight, and the density of the bulk species.

3.2 Plasma boundary conditions

The electron flow into the reactor wall is determined by:

$$-\mathbf{n} \cdot \mathbf{\Gamma}_{e} = \left(\frac{1}{2} \nu_{e, th} n_{e}\right) - \sum_{p} \gamma_{p} (\mathbf{\Gamma}_{p} \cdot \mathbf{n}), \tag{23}$$

$$v_{\rm e,th} = \sqrt{\frac{8K_{\rm B}T_{\rm e}}{\pi m_{\rm e}}},$$
 (24)

where $v_{e,th}$, K_B , and **n** represent, respectively, the thermal electron velocity, the Boltzmann constant, and the normal unit vector. y_n is the coefficient of the secondary emission.

Electrons transfer energy to walls through:

$$-\mathbf{n}\cdot\mathbf{\Gamma}_{\varepsilon} = \left(\frac{5}{6}\nu_{e,\text{th}}n_{e}\right). \tag{25}$$

As a result of surface reactions, heavy species lose ions to the wall since the electric field is directed toward the wall [25].

$$-\mathbf{n} \cdot \mathbf{j}_{k} = M_{\omega} R_{k} + M_{\omega} e_{k} Z \mu_{k} (\mathbf{E} \cdot \mathbf{n}) [Z_{k} \mu_{k} (\mathbf{E} \cdot \mathbf{n}) > 0]. \quad (26)$$

Here, (**E·n**) and (**n·** j_k) are the normal components of the wall of the electric field and the heavy species current density, respectively. e_k and M_ω represent the elementary charge of the species k and the mass of the ionic species, respectively. In addition, the reactor walls are grounded.

3.3 Chemical model

Identification of species and reactions in plasma chemistry is critical. The species and reaction used for inductively coupled oxygen plasma enhanced atomic layer deposition are taken from the study of Christophorou and Olthoff [26]. The chemical model includes electrons and 11 different oxygen species, such as O_2 , O_1 , O_2^+ , O_2^- , O_2^+ , O_2^- , O_2^* (1D), $O^*(1S)$, $O_2^*(v)$, $O_2^*(1\Delta)$, and $O_2^*(1\Sigma)$. In this case, the $O^*(1S)$ and O*(1D) states are the atomic oxygen exciting states. The vibrationally excited state of O₂ is represented by O₂*(v), which refers to the O245 state. The excited states of molecular oxygen are given by (O2a1d) and (O2b1s), which refer to $O_2^*(1\Delta)$ and $O_2^*(1\Sigma)$, respectively. O_3 is not included in the model since it has a minor effect on these plasma types [27]. A total of 62 reactions are included in the model [24]. The electron impact reaction rates are given in the study of Kropotkin and Voloshon [28,29].

The reactor walls neutralize and reflect all the O^+ , O^- , and O_2^+ ions in the plasma. In addition, $O^*(1D)$, $O^*(1S)$, $O_2^*(v)$, $O_2^*(1\Delta)$, and $O_2^*(1\Sigma)$ are returned to the ground state after being de-excited and reflected back into the plasma after colliding with the wall. A reaction rate of 0.2 is assumed for atomic oxygen to recombine at the wall to produce O_2 [30].

3.4 Geometry of the discharge model

Figure 2 (right) illustrates the simulated geometry. Plasma is confined in a vacuum chamber mounted by a metal electrode and a five-turn planar copper coil antenna. Using a quartz cylinder (1 cm thick and 3.2 cm in radius), electrical power is inductively coupled to the plasma volume. A grounded electrode with a radius of 4.12 cm and made of stainless steel is used. The quartz cylinder and the lower electrode are separated by a space of 4 cm. Oxygen gas is injected into the discharge volume at 400 W applied power with 13.56 MHz sinusoidal frequency and pressures between 3 and 100 Pa. Figure 2 (left) shows the meshing of the reference cell with 14,460 triangular elements.

3.5 Computational process

COMSOL Multiphysics is used to implement a 2D axisymmetric simulation model of ICP generated in a GEC reference cell reactor [31]. Models with axial symmetry perform better than their isotropic counterparts. Nonetheless, due to its inability to scale, the axisymmetric-based approach is impractical when dealing with large data sets. As a result, subsampling or providing computationally practical likelihood estimates is necessary [32]. It is typically found that inductively coupled discharges generated at low pressure provide high charge densities (>10¹⁶ m⁻³) [33,34]. Furthermore, surface anisotropy is achieved with low pressure ion bombardment, which makes high density plasma sources appealing. The negative ion temperature is equal to 0.3 eV

when calculating negative ion mobility and diffusivity since the ions are held within the plasma core, where they acquire energy from the electromagnetic field at high frequencies [35,36]. Three steps are involved in calculating plasma properties. As a first step, the electromagnetic field inside the discharge reactor must be determined using Maxwell's equations. In the second step, based on these fields, Boltzmann solvers are used to determine electron energy distribution functions and electron impact reaction rates. In the third step, on the basis of the reaction rates, different species of oxygen plasma gas and distribution of electron density are determined. Finally, electromagnetic fields are re-calculated based on the electrostatic field derived from Poisson's equation, and the calculation loop is closed. An iterative process is carried out until a model is convergent. The model simulation requires a 64bit machine with at least 4 GB of memory because of the large number of reactions and species.

4 Results and discussion

A GEC reactor is used to study inductively coupled plasmaenhanced plasma laser deposition (PE-PLD). The plasma discharge is sustained at a temperature of 500 K by operating at 13.56 MHz [37]. The results of the modeling are compared with those of the experiments. The influence of implemented power and gas pressure on the quality of the metal oxide films is examined in this section. Working power from 100 to 1,000 W and gas pressure from 0.5 to 100 Pa (3 to 750 mTorr) are considered.

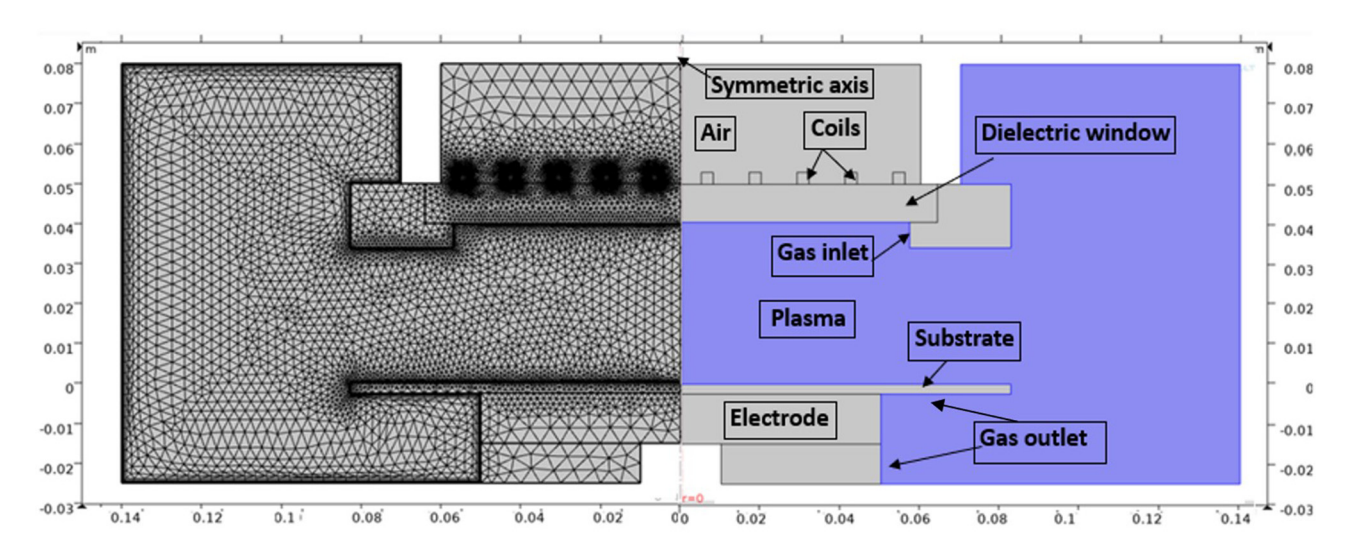


Figure 2: Cell coupled GEC reference structure (right) and structure meshing of GEC-ICP (left).

4.1 Validation of the numerical model

Figure 3 shows the variation of electron density with the applied power at various pressures 0.5, 7, and 14 Pa (3, 50, and 100 mTorr) in inductively coupled oxygen plasma. The results are compared with the experimental electron density obtained from the literature [38] using a Langmuir probe with uncertainty measurements between 5 and 10%. There is a linear relationship between electron density and power, while a weak decrease of electron density is observed with pressure. The agreement is good; however, the chemical model did not adjust experimental chemical coefficient rates and there are no inelastic electron collisions, which can explain the simple disagreement between simulation and experiment.

4.2 Reactive oxygen plasma

Figure 4 presents the 2D spatial distribution in electron density, electron temperature, collisional power loss, electric potential, and velocity field in the discharge volume at 400 W power, 10 Pa (75 mTorr) pressure, and oxygen gas.

The maximum electron density is about $1.21 \times 10^{18} \, \mathrm{m}^{-3}$ and is located at the center of the reactor under the RF coil (Figure 4a). Azimuthal electric field shielding occurs and is high in this case because of the density of electrons. The temperature of electrons is displayed in Figure 4b. In the reactor center, the density of electrons and temperature are elevated, and the dissipated power (Figure 4c) is increased at $0.77 \times 10^6 \, \mathrm{W/m^3}$. Most power deposition occurs

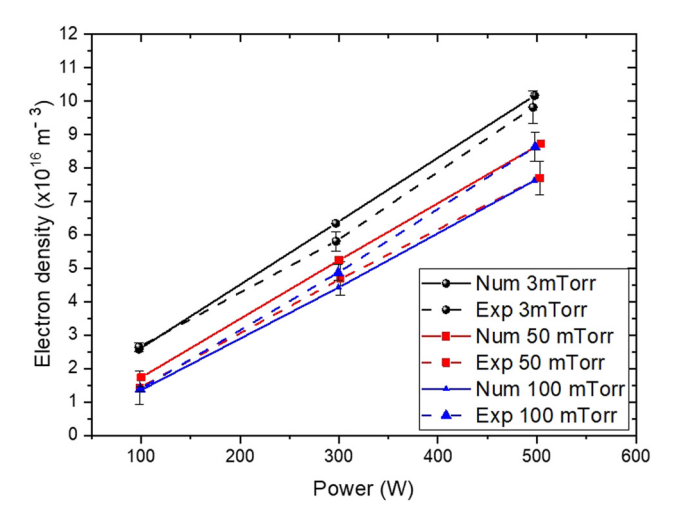


Figure 3: Variation of numerical and experimental electron densities with the applied power in RF-inductively coupled oxygen plasma.

at an arc length of 35 mm below the third and fourth coils of the reactor. Figure 4d displays the distribution of electric potential, and Figure 4e presents the velocity field, where gas cannot penetrate deep into the plasma core at these flow rates. Through the pump, the gas flows down toward the wafer, then around it, and out to the pump. Gas flow has a relatively small effect on ICPs which operate at very low pressures.

The surface distribution of reactive oxygen density at 400 W RF input power and 10 Pa (75 mTorr) is shown in Figure 5. The distributions of charged particles (electrons, 0^+ , 0^- , and 0_2^+) indicate that most of the power is dissipated just below the coil, in front of the quartz cylinder. The predominant positive oxygen ion is 0^+ , with a maximum density of $1.17 \times 10^{18} \, \text{m}^{-3}$. 0_2^+ has a density that is nearly two orders of magnitude lower. Due to the presence of a considerable number of negative ions 0^- , the plasma is electronegative.

The neutral oxygen atom (O), excited atomic oxygen species (O*(1D) and O*(1S)), and excited molecular oxygen species (O2*(1 Δ), O2*(1 Δ), and O2*(v)) identified in the model as O2a1d, O2b1s, and O245, respectively, have peak densities that are two or three orders of magnitude higher than those of charged particles [39]. In addition, the neutral species distribution across the inter-electrode gap is more homogeneous. These reactive neutral species dominate the impact of charged particles in PE-PLD, emphasizing higher importance in thin film deposition. The singlet delta oxygen O2*(1 Δ) identified as O2a1d and atomic oxygen (O) are chemically highly reactive. So, in PLDs with an O2 gas background, these species are critical in thin film deposition.

Plasma plumes as well as background gases react to create reactive O and $O_2^*(1\Delta)$ species. As a result, reactive oxygen species are directly correlated with the ablation process limiting the control of reactive oxygen species properties [40].

 O^- ions have a higher density than O_2^- ions, since O_2 is produced by the dissociative attachment reaction (e + $O_2 \rightarrow O^-$ + O) which is greater than the three-body attachment reaction (e + $2O_2 \rightarrow O_2 + O_2^-$).

Figure 6 illustrates the axial distribution of oxygen density at 400 W-RF and varied O₂ pressures of 10 Pa (75 mTorr) and 50 Pa (375 mTorr). In Figure 6a, a doughnut shape is formed by the charged species, which is even more localized in front of the quartz cylinder in the 10 Pa case. In Figure 6b, the reactor-averaged density of all charged species is higher at 50 Pa than at 10 Pa. Reactive neutral oxygen atom species have lower peaks, and reactor average densities are reduced by a factor of 10 orders for O. The maximum oxygen species densities are localized under the quartz window.

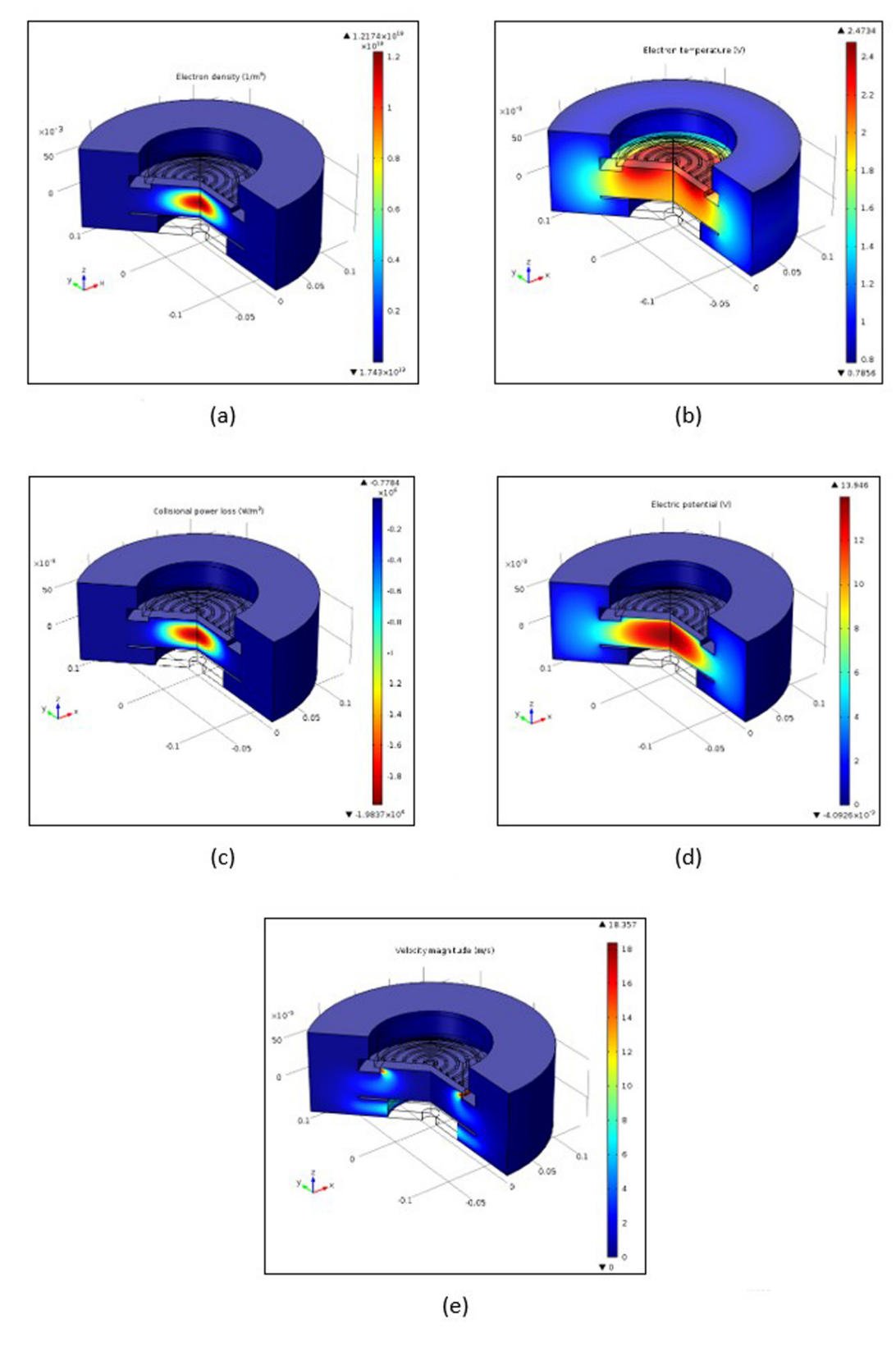
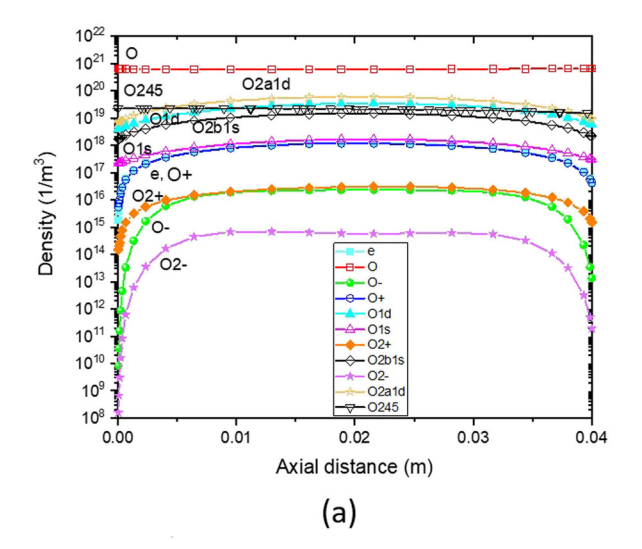


Figure 4: 2D distribution of (a) electron density, (b) electron temperature, (c) collisional power loss, (d) electric potential, and (e) velocity field.

Figure 5: Surface distribution of reactive oxygen plasma (electron, O_2 , O, O_2^+ , O^+ , O_2^- , O^- , O_2^+ , O^+ , O_2^- (1 Δ), O_2^* (v), and O_2^* (1 Σ)) in 10 Pa oxygen gas at 400 W in a GEC-ICP reactor.



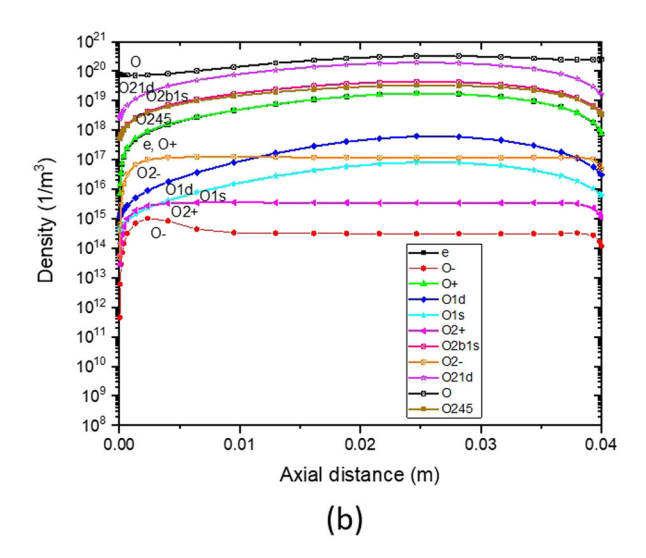
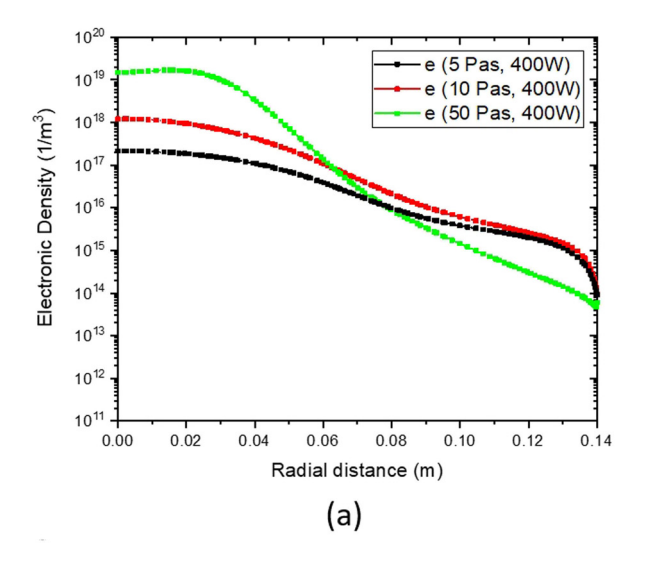


Figure 6: Axial density distribution in reactive oxygen gas (electron, O_2 , O_2 ,

 ${\rm O_2}^*,~{\rm O}^*,~{\rm and}~{\rm O}$ are no longer homogeneously distributed across the reactor. They are localized in the same region as the charged species. During the PLD process, the oxygen content is optimized by exploring these differences in density with pressure.

During deposition, oxygen atoms are generated by both the target and collisions in the plasma plume and have a greater oxidation power compared to molecular oxygen [41]. Figure 7 shows the evolution of oxygen atoms O and electron density under various pressures. Figure 7a shows that the electron density varies linearly with pressure. Figure 7b shows that with increasing pressure, the oxygen atom density increases and then decreases.

To explain more the variation of atomic oxygen density with pressure, the pressure is varied between 3 and 100 Pa (22–750 mTorr), which is a suitable domain to activate the deposition substrate. Figure 8 displays the density distribution of oxygen atoms and metastable molecular oxygen close to the metal electrode. It indicates that the $\rm O_2^*$ density increases from 4 × 10¹³ cm⁻³ to 1 × 10¹⁵ cm⁻³ when the pressure is increased from 3 Pa to 100 Pa. In contrast, O exhibits a different behavior with pressure, varying between 3 × $\rm 10^{13}\,cm^{-3}$ and 2 × $\rm 10^{14}\,cm^{-3}$, with an elevated density at 10 Pa (75 mTorr) and the lowest at 100 Pa. Hence, the dominant species at 3 Pa is O, which has a density that is twice as high as $\rm O_2^*$. By increasing the pressure to 100 Pa, the



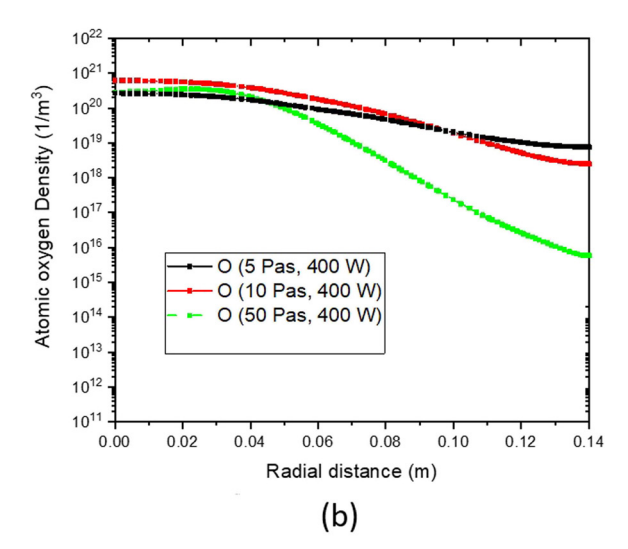


Figure 7: Radial distribution of (a) electron density and (b) atomic oxygen density for different pressures.

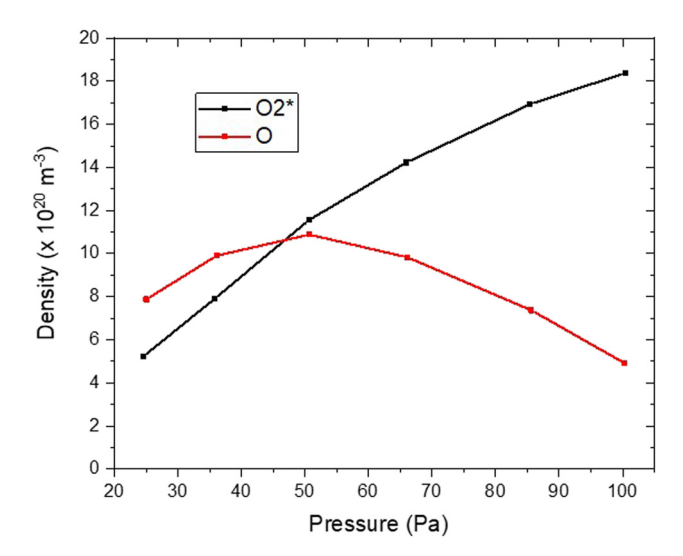


Figure 8: Density distribution of O₂* and O with pressure in front of the lower electrode.

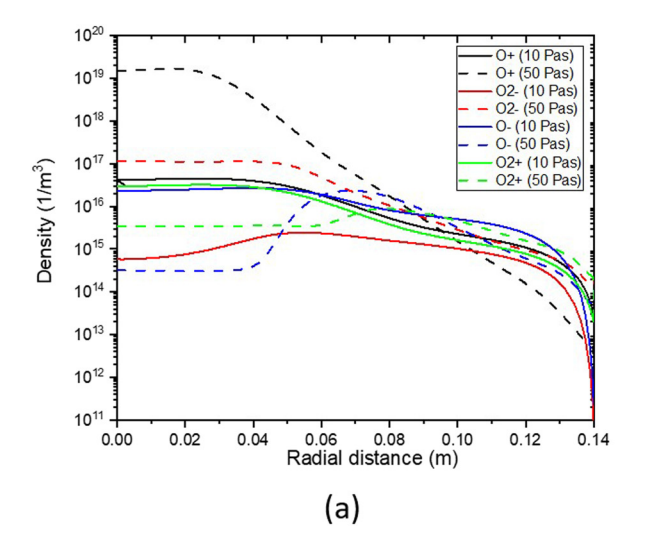
dominant reactive species is O_2 . This change in reactive oxygen species impacts on thin film properties. A similar result is found in simulations by Blackwell *et al.* [42], wherein the crystal composition, stoichiometry, and quality of metal oxide films are affected by the O/O_2 ratio.

The plasma medium has a high density of ionized particles which affects its diagnosis. Figure 9 illustrates the radial distribution of charged and metastable species of oxygen gas with 400 W input power at 10 Pa (75 mTorr) and 50 Pa (375 mTorr). The peaks of reactive ion oxygen density increase with pressure. Also, with increasing pressure, the ion drift flux depending on the electron temperature and the diffusion flux of ions decline together, resulting in a decline of the total ion flux.

Figure 10 shows how charged, neutral, and metastable oxygen species density evolve with applied power. In Figure 10a, electron densities vary linearly with power. This trend is also supported by experiments [43]. According to Figure 10b, increasing the power values under the RF coil increases the density of excited oxygen atoms and oxygen molecules. Increasing power causes oxygen atoms to gain energy, leading to higher atom excitation.

The electron temperature and ion density are important parameters influencing the deposition of oxide thin films. The electron temperature is proportional to bombardment energy, causing oxide films homogeneity defect. Furthermore, ion density affects the deposition rate. Hence, the oxygen ion density and electron temperature in Figure 11 are displayed as functions of power and pressure in the middle of the reactor. Figure 11a illustrates the applied power affecting the ion density and electron temperature at 10 Pa (75 mTorr). As the applied power increases between 100 and 600 W, the oxygen ion density increases and the electron temperature decreases. Increasing power causes higher ionization rates, which result in a plasma rich in electrons and ions. While a decline in the electron temperature is observed in the plasma zone because of energy loss [44,45].

According to Figure 11b, when the pressure varies from 10 to 40 Pa (75 to 300 mTorr), the oxygen ion density increases, while the electron temperature decreases. Furthermore, the oxygen density in the plasma region becomes higher as the pressure rises. As collisions increase at high pressure, particles per unit volume increase [46,47]. A proportional increase in collision rate with pressure results in energy loss by collisions, which lowers the temperature of electrons. There is an agreement between these



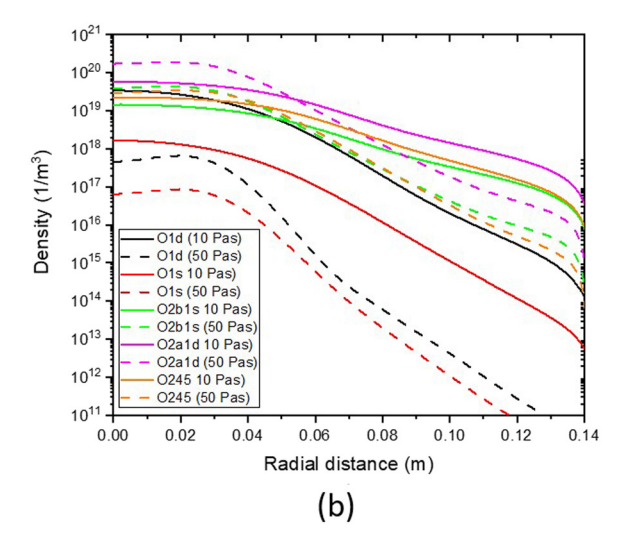
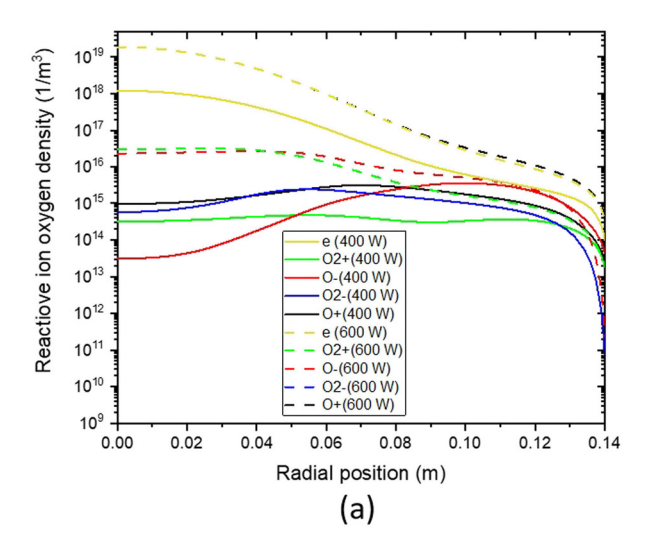


Figure 9: Radial distribution of (a) oxygen particles and (b) metastable oxygen particles for different pressures at z = 0.02 m with 400 W input power.



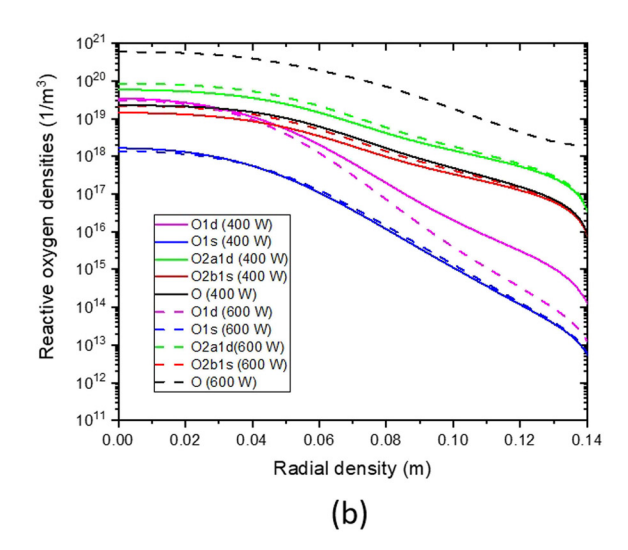


Figure 10: Radial distribution of densities of (a) oxygen particles and (b) neutral oxygen particles for different powers at z = 0.02 m with 10 Pa pressure.

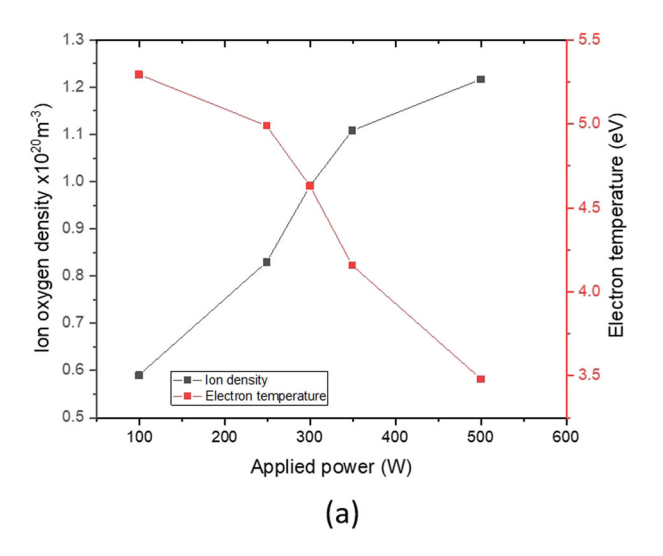
results and those of Ojeda *et al.* [48] in terms of density and electron temperature.

A simulation of oxide film growth rate in response to applied power and gas pressure is presented. Figure 12 shows how applied power affects ZnO film deposition rates for different operating pressures. With increasing power and pressure, the deposition rate increases almost linearly [49].

4.3 Correlation analysis

This article focuses on the growth of metal oxide thin films on a polymer substrate through PE-PLD to overcome some limitations of the conventional PLD method, such as the need to use multi-element targets and elevated substrate temperatures. The standard PLD setup with a metal target will be combined with an electrically produced low-temperature oxygen background plasma. Crucially, oxygen plasma is a pulsed non-equilibrium plasma to maintain a low temperature, which prevents the substrate from being significantly heated by the plasma's conductivity and enables the deposition of coatings onto delicate substrates.

The results show that the direct contact between the active plasma and the ablation plume results in more reactive, energetic plasma particles impinging on the substrate, instead of an afterglow plasma beam. In contrast, in the plasma beam assisted PLD system presented by Dinescu



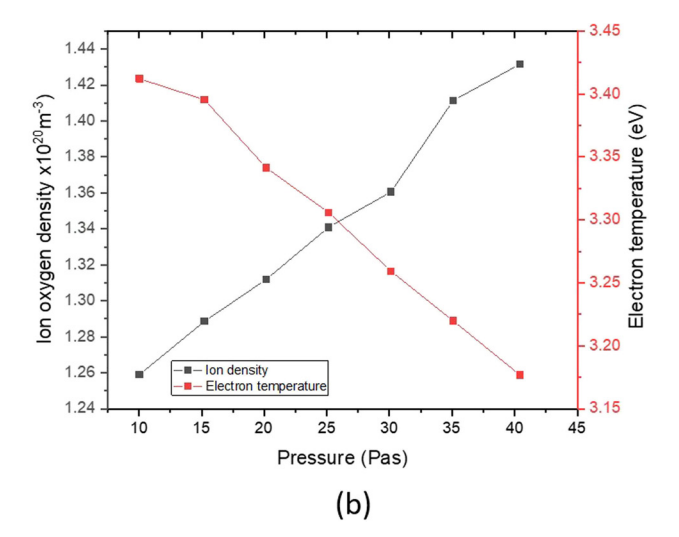


Figure 11: Ion oxygen density and electron thermal distribution in films deposited by PE-PLD under different (a) applied powers and (b) pressures of the ICP.

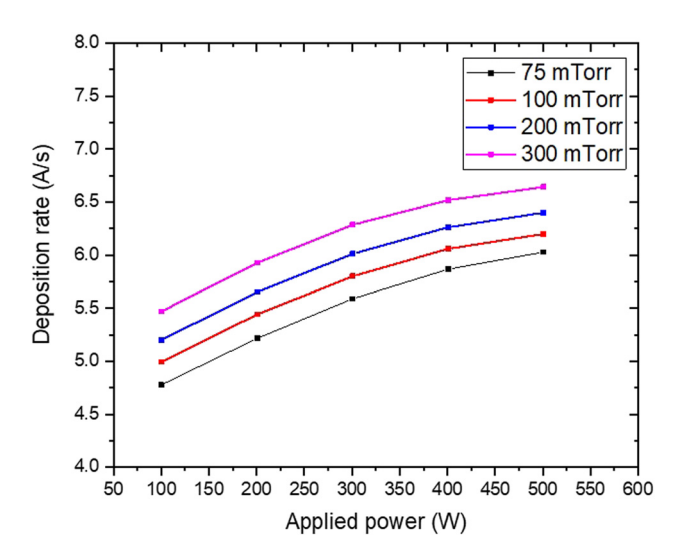


Figure 12: Variation of deposition rate with applied power at different values of pressure.

et al. [17], an additional oxygen plasma beam impinges on the substrate to form ZnO films. This system provides highquality ZnO films only when combined with 800 K substrate heating.

In addition, since these particles are more energetic in PE-PLD than an afterglow plasma or a neutral background gas, where electrons present a high temperature proportional to the energy of bombardment of the substrate, their diffusion lengths are longer, resulting in more crystalline films [50].

A background plasma plume also provides particles for a longer period of time than a laser-produced plume. As a result, polycrystalline films can be deposited at room temperature because incoming particles are more likely to find good sites on the surface for crystalline growth. Our results are in accordance with the work of Tricot *et al.* [51], which concludes that using pulsed-electron beam deposition systems delivers plasma species to substrates for much longer periods of time than conventional PLD systems.

In addition, De Giacomo $et\ al.\ [52]$ studied TiO_2 films made via PE-PLD, while Huang $et\ al.\ [15]$ reported ZnO films deposited at ambient temperature using the RF-PE-PLD technique. These systems similar to our work use a plasma backdrop to decrease the droplets in the PLD plume rather than using the background plasma to provide oxygen for the film.

5 Conclusions

The use of PE-PLD for metal oxide thin film deposition is presented in this article. Cold oxygen plasma is used

instead of neutral gas to enhance process control and check polymer stability issues. A two-dimensional model of an RF-inductively coupled oxygen plasma is developed using COMSOL Multiphysics to understand the dynamics of inductively coupled oxygen discharge. The electron density, electron temperature, electric potential, as well as oxygen ion and excited oxygen atom densities are calculated inside the GEC-ICP reference cell reactor. According to simulation results, a low-pressure RF-ICP plasma generates significant quantities of reactive oxygen species including O and O₂, at densities of up to 10¹⁹ m⁻³, compared to a conventional oxygen gas background. Due to the similar density of these plasma plumes and background plasma, it appears plausible that similar rates of oxygen and metal deposition can result. The temperature of electrons is proportional to the energy of bombardment. As a result, the substrate receives chemical energy from the oxygen plasma to enhance the growth of the film without the need for further substrate heating. PE-PLD has comparable stoichiometry and crystallinity to PLD, but it does not heat the substrate and uses pure metal targets instead of metal oxide ones. Metal oxide films were polycrystalline, and their stoichiometry could be adjusted by adjusting the ICP power. The results show that densities of electrons, excited oxygen atoms, and oxygen ions increase with power. However, the electric potential and electron temperature decrease as the input power increases and increasing power causes oxygen atoms to gain energy, leading to higher atom excitation. Moreover, the oxygen gas pressure plays a crucial role in determining the properties of films. As the pressure increases, the oxygen ion density increases and the electron temperature decreases, which enhance the deposition rate. In contrast to O_2 , the O_3 density decreases at pressures above 10 Pa.

The film deposition is significantly affected by reactive species O and O_2 , and the results show that with increasing power and pressure, the deposition rate increases almost linearly.

PE-PLD is a powerful method with a wide range of uses in several domains. Its accuracy and adaptability make it a useful instrument for engineers and researchers, propelling developments in fields like technology, healthcare, and energy.

Acknowledgments: This research project was funded by the Deanship of Scientific Research and Libraries, Princess Nourah bint Abdulrahman University, through the Program of Research Project Funding After Publication, grant no. RPFAP-63-1445.

Funding information: This research project was funded by the Deanship of Scientific Research and Libraries, Princess

Nourah bint Abdulrahman University, through the Program of Research Project Funding After Publication, grant no. RPFAP-63-1445.

Author contributions: Samira Elaissi and Norah A.M. Alsaif - methodology, writing, supervision, project management, and data revision. All authors have accepted responsibility for the entire content of this manuscript and approved its submission.

Conflict of interest: The authors state no conflict of interest.

Data availability statement: All data generated or analyzed during this study are included in this published article.

References

- Devaraj P, Peranantham P, Devarani Devi K, Siva Kumar VV, Jeyachandran YL. Oxidation characteristics of copper oxide thin films deposited by direct current sputtering under substrate temperature and post-deposition copper-ion implantation. Thin Solid Films. 2024;804:140485.
- Patil PR, Borse HP, Chaware NP, Huse DNP. Study of optoelectronic properties of ZnO thin film grown by facile solution growth technique. Int | Sci Res Sci Techn. 2024;11(9):322-9.
- Fasquelle D, Députier S, Bouquet V, Guilloux-Viry M. Effect of the microstructure of ZnO thin films prepared by PLD on their performance as toxic gas sensors. Chemosensors. 2022;10(7):285.
- Rakhimkulov S, Absattorov D, Borikhonov B, Yakubov E. Synthesis and application of zinc oxide nanoparticles. Res J Chem Env. 2024;28(1):1-20.
- Dosmailov M, Leona LN, Patek J, Roth D, Bauer P, Scharber MC, et al. Transparent conductive ZnO layers on polymer substrates: Thin film deposition and application in organic solar cells. Thin Solid Films. 2015;591(Part A):97-104.
- Zaier A, Meftah A, Jaber AY, Abdelaziz AA, Aida MS. Annealing effects on the structural, electrical and optical properties of ZnO thin films prepared by thermal evaporation technique. J King Saud Univ Sci. 2015;27(4):356-60.
- Faramawy A, Elsayed H, Scian C, Mattei G. Structural, optical, magnetic and electrical properties of sputtered ZnO and ZnO: Fe Thin films: The role of deposition power. Ceramics. 2022;5(4):1128-53.
- Tiwari C, Pandey A, Dixit A. Precursor mediated and defect engineered ZnO nanostructures using thermal chemical vapor deposition for green light emission. Thin Solid Films. 2022;762:139539.
- [9] Haider AJ, Jabbar AA, Ali GA. Pure and doped ZnO nanostructure production and its optical properties using pulsed laser deposition technique. J Phys: Conf Ser. 2021;1795:012015.
- [10] Escalona M, Bhuyan H, Valenzuela JC, Ibacache S, Wyndham E, Favre M, et al. Comparative study on the dynamics and the

- composition between a pulsed laser deposition (PLD) and a plasma enhanced PLD (PE-PLD). Results Phys. 2021;24:104066.
- [11] Hacini N, Ghamnia M, Dahamni MA, Boukhachem AB, Pireaux JJ, Houssiau L. Compositional, structural, morphological, and optical properties of ZnO thin films prepared by PECVD technique. Coatings. 2021;11(2):202.
- Rajendiran S, Meehan D, Wagenaars E. Plasma-enhanced pulsed laser deposition of copper oxide and zinc oxide thin films. AIP Adv. 2020;10(6):065323.
- [13] Bukharia SA, Kumarb S, Kumarc P, Gumfekara SP, Chunga HJ, Thundata T, et al. The effect of oxygen flow rate on metal-insulator transition (MIT) characteristics of vanadium dioxide (VO2) thin films by pulsed laser deposition (PLD). Appl Surf Sci. 2020;529:146995.
- [14] Chou CM, Lai CC, Chang CW, Wen KH, Hsiaom VKS. Radio-frequency oxygen-plasma-enhanced pulsed laser deposition of IGZO films. AIP Adv. 2017;7:075309.
- [15] Huang SH, Chou YC, Chou CM, Hsiao VKS. Room temperature radiofrequency plasma-enhanced pulsed laser deposition of ZnO thin films. Appl Surf Sci. 2013;226:194-8.
- [16] Scarisoreanu N, Matei DG, Dinescu G, Epurescu G, Ghica C, Nistor LC, et al. Properties of ZnO thin films prepared by radiofrequency plasma beam assisted laser ablation. Appl Surf Sci. 2005;247(1-4):518-25.
- [17] Nistor LC, Ghica C, Matei D, Dinescu G, Dinescu M, Van Tendeloo G. Growth and characterization of a-axis textured ZnO thin films. J Cryst Growth. 2005;277(1-4):26-31.
- [18] COMSOL Multiphysics® v.5.1. www.comsol.com. COMSOL AB, Stockholm, Sweden.
- [19] Zhang CY, Zhong XL, Wang JB, Yang GW. Room-temperature growth of cubic nitride boron film by RF plasma enhanced pulsed laser deposition. Chem Phys Lett. 2003;370(3-4):522-7.
- [20] Siari K, Rebiai S, Bahouh H, Bouanaka F. Plasma-enhanced chemical vapor deposition of silicon films at low pressure in GEC reference cell. Plasma Phys Rep. 2020;46:667-74.
- Ramamurthi B, Economou DJ. Pulsed-power plasma reactors: Twodimensional electropositive discharge simulation in a GEC reference cell. Plasma Sources Sci Technol. 2002;11(3):324-32.
- [22] Hagelaar GJM, Pitchford LC. Solving the Boltzmann equation to obtain electron transport coefficients and rate coefficients for fluid models. Plasma Sources Sci Technol. 2005:14:722-33.
- [23] Jaeger EF, Berry LA, Tolliver JS, Batchelor DB. Power deposition in high-density inductively coupled plasma tools for semiconductor processing. Phys Plasmas. 1995;2:2597.
- [24] Kropotkin A, Chukalovsky A, Kurnosov A, Rakhimova T, Palov A. Modelling of an icp discharge in oxygen with full kinetics scheme with newly calculated vv/vt rate constants. Publ Astron Obs Belgrade. 2024;103:130-3.
- [25] Application Gallery: Model of an Argon/Oxygen inductively coupled plasma reactor [Internet]. COMSOL Multiphysics® v.5.1. www. comsol.com. COMSOL AB, Stockholm, Sweden; 2025 [cited 2025 May 10]. https://www.comsol.com/model/model-of-anargonoxygen-inductively-coupled-plasma-reactor-109191.
- Christophorou GL, Olthoff JK. Fundamental electron interactions with plasma processing gases. 2nd edn. New York: Springer; 2003.
- Koster G, Blank DHA, Rijnders GAJHM. Oxygen in complex oxide thin films grown by pulsed laser deposition: A perspective. J Supercond Nov Magn. 2020;33:205-12.
- [28] Kropotkin AN, Voloshin DG. ICP argon discharge simulation: The role of ion inertia and additional RF bias. Phys Plasmas. 2020;27(5):053507.

- [29] Miller PA, Hebner GA, Greenberg KE, Pochan PD, Aragon BP. An inductively coupled plasma source for the gaseous electronics conference RF reference cell. J Res Natl Inst Stand Technol. 1995;100(4):427.
- [30] Wang J, Rijnders G, Koster G. Complex plume stoichiometry during pulsed laser deposition of SrVO3 at low oxygen pressures. Appl Phys Lett. 2018;113(22):223103.
- [31] Seadawy AR. Ion acoustic solitary wave solutions of twodimensional nonlinear Kadomtsev–Petviashvili–Burgers equation in quantum plasma. Math Method Appl Sci. 2017;40(5):1598–607.
- [32] Porcu E, Castruccio S, Alegría A, Crippa P. Axially symmetric models for global data: A journey between geostatistics and stochastic generators. Environmetrics. 2019;30(1):e2555.
- [33] Seadawy AR. Stability analysis solutions for nonlinear threedimensional modified Korteweg–de Vries–Zakharov–Kuznetsov equation in a magnetized electron–positron plasma. Phys A. 2016:455:44–51.
- [34] Seadawy AR. Solitary wave solutions of two-dimensional nonlinear Kadomtsev-Petviashvili dynamic equation in dust-acoustic plasmas. Pramana - | Phys. 2017;89:49.
- [35] Abdullah A, Seadawy AR, Wang J. Stability analysis and applications of traveling wave solutions of three-dimensional nonlinear modified Zakharov–Kuznetsov equation in a magnetized plasma. Mod Phys Lett A. 2018;33(25):1850145.
- [36] Cheemaa N, Seadawy AR, Chen S. Some new families of solitary wave solutions of the generalized Schamel equation and their applications in plasma physics. Eur Phys J Plus. 2019;134(117):12467.
- [37] Ponnamma D, Cabibihan JJ, Rajan M, Pethaiah SS, Deshmukh K, Gogoi JP, et al. Synthesis, optimization and applications of ZnO/ polymer nanocomposites. Mat Sci Eng C-Solid. 2019;98:1210–40.
- [38] Kiehlbauch MW, Graves DB. Inductively coupled plasmas in oxygen: Modeling and experiment. J Vac Sci Technol A. 2003;21(3):660–70.
- [39] Rajendiran S, Rossall AK, Gibson A, Wagenaars E. Modelling of laser ablation and reactive oxygen plasmas for pulsed laser deposition of zinc oxide. Surf Coat Tech. 2014;260:417–23.
- [40] Singh J, Srivastava PK, Siwach PK, Singh HK, Tiwari RS, Srivastava ON. PLD deposited ZnO films on different substrates and oxygen pressure: A study of surface morphology and optical properties. Sci Adv Mater. 2012;4(3–4):467–74.

- [41] Chou CM, Lai CC, Chang CW, Wen KS, Hsiao VKS. Radio-frequency oxygen-plasma-enhanced pulsed laser deposition of IGZO films. AIP Adv. 2017;7:075309.
- [42] Blackwell S, Smith R, Kenny SD, Walls JM, Sanz-Navarro CF. Modelling the growth of ZnO thin films by PVD methods and the effects of post-annealing. J Phys Condens Matter. 2013;25:135002.
- [43] Marza HH, Khalaf TH. The effect of power on inductively coupled plasma parameters. Iraqi | Phys. 2022;20(3):98–108.
- [44] Gu Y, Li X, Yu W, Gao X, Zhao J, Yang C. Microstructures, electrical and optical characteristics of ZnO thin films by oxygen plasma-assisted pulsed laser deposition. J Cryst Growth. 2007;305(1):36–9.
- [45] Orsel K. Analysis of transient plasmas for pulsed laser deposition using spatiotemporally resolved laser-induced fluorescence. PhD dissertation. Enschede, The Netherlands: University of Twente: 2016.
- [46] Escalona M, Bhuyan H, Ibacache S, Retamal MJ, Saikia P, Borgohain C, et al. Study of titanium nitride film growth by plasma enhanced pulsed laser deposition at different experimental conditions. Surf Coat Tech. 2020;405:126492.
- [47] Bogaerts A, Chen Z. Effect of laser parameters on laser ablation and laser-induced plasma formation: A numerical modeling investigation. Spectrochim Acta B. 2005;60(9–10):1280–307.
- [48] OjedaGP A, Schneider CW, Lippert T, Wokaun A. Pressure and temperature dependence of the laser-induced plasma plume dynamics. J Appl Phys. 2016;120(22):225301.
- [49] Wise RS, Lymberopoulos DP, Economou DJ. Rapid two-dimensional self-consistent simulation of inductively coupled plasma and comparison with experimental data. Appl Phys Lett. 1996;68(18):2499–501.
- [50] Nistor M, Mandache NB, Perrière J. Pulsed electron beam deposition of oxide thin films. J Phys D: Appl Phys. 2008;41:165205.
- [51] Tricot S, Boulmer-Leborgne C, Nistor M, Millon E, Perrière J. Dynamics of a pulsed-electron beam induced plasma: application to the growth of zinc oxide thin films. J Phys D: Appl Phys. 2008:41:175205.
- [52] De Giacomo A, Shakhatov V, Senesi GS, Orlando S. Spectroscopic investigation of the technique of plasma assisted pulsed laser deposition of titanium dioxide. Spectrochim Acta B. 2001;56(8):1459–72.